

CHAPTER 8

GNSS reflectometry (GNSS-R) for environmental observation

The foundations behind the utilization of reflected GNSS signals for environmental research were laid down in the 1990s. Several pioneering works laid the groundwork for using these “signals of opportunity.” Martin-Neira proposed the Passive Reflectometry and Interferometry System (PARIS) for using signals of opportunity for ocean altimetry (Martin-Neira, 1993). The developed methodologies can be classified into categories, based on platforms and signals used. The platform classification includes spaceborne, airborne, and ground-based techniques. Classification based on the signal property includes Doppler-delay map (DDM), signal-to-noise ratio (SNR), and carrier-phase observation techniques. In terms of receiving station’s setups, there are upward-looking and side-looking single-antenna setups, as well as dual-antenna setups, i.e., one upward-looking and one side- or downward-looking antenna. Each technique is briefly described in this chapter. These techniques enable the measurement of (1) wind speed over water bodies (see “GNSS-R wind speed measurements” section), (2) water level height including sea level (see “GNSS-R water level/land height measurements” section) and land elevation, (3) soil moisture (“GNSS-R soil moisture monitoring” section), (4) vegetation, and (5) snow height observations (see Fig. 8.1).

Spaceborne GNSS Reflectometry resembles the Synthetic-Aperture Radar (SAR) methodology of probing the Earth’s surface. In SAR systems the transmitter and receiver are situated on the same satellite, orbiting the Earth, and use the same antenna (these systems are known as monostatic radar systems). The SAR satellites usually operate in LEO and, in general, provide data on the distance traveled by the signal from the transmitter, reflected by the Earth’s surface and back to the onboard receiver. The GNSS-R satellite measurements can be categorized as multistatic radars. Conceptually, the signal transmitted from the MEO GNSS satellites is reflected from the Earth’s surface and then received by an LEO satellite. Unlike SAR, each GNSS-R LEO satellite can observe reflections from

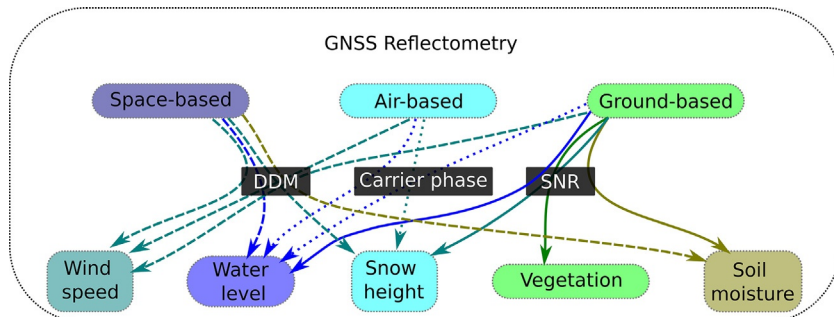


Fig. 8.1 GNSS overview. Overview of the GNSS-R platforms, methods, and applications. The arrows connect each platform with the measured environmental property through the used methodology (solid lines indicate SNR, dashed lines—DDM's, and dotted—carrier phase methods).

multiple MEO GNSS satellites simultaneously, but the receiving satellite has no control over the direction from which the reflections are coming.

Theoretical background—Polarization

When an electromagnetic wave is reflected from a surface, the wave interacts with the reflective surface in accordance with Brewster's law. Brewster's law states that an unpolarized electromagnetic wave reflected above a certain threshold incidence angle is known as Brewster angle (Fig. 8.2).

$$\theta = \arctan \left(\frac{n_1}{n_2} \right), \quad (8.1)$$

The electromagnetic wave polarized in the same plane as the incident electromagnetic wave and the surface normal at the point of incidence is not reflected.

When the right-hand circular polarized (RHCP, see Chapter 2) GNSS signals are reflected from the surface of the Earth, they are subject to Fresnel's reflectivity relationship

$$E_p = R_{pq} E_q, \quad (8.2)$$

where E_p is the electric field of the scattered signal with polarization p , E_q is the incidence electric field with polarization q , and R_{pq} is the Fresnel coefficient for q - to p -polarized reflection. This coefficient depends on the dielectric properties of the reflective surface, as well as on the incident angle. For each polarization pair, the R coefficient is different. The sum of the R coefficients for any reflection is $R < 1$, since the reflection cannot generate

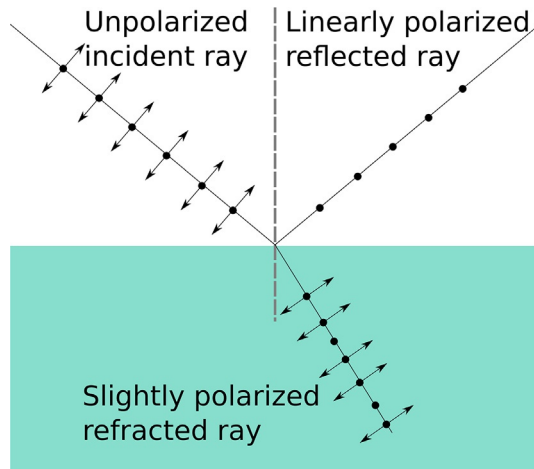


Fig. 8.2 Brewster. Unpolarized signal, approaching a reflective surface at incidence angles larger than the Brewster angle, is polarized at reflection with linear polarization, perpendicular to the plane, defined by the incoming signal and the normal of the reflective surface. (Reproduced from https://en.wikipedia.org/wiki/Brewster%27s_angle#/media/File:Brewsters-angle.svg.)

an electric field stronger than the incidence (Conservation law). Eq. (8.2) shows that part of the reflected electromagnetic wave changes its polarization upon reflection, while part of it maintains its polarization.

The portion of the reflected GNSS signal, which maintains its RHCP polarization, depends on the Brewster law. When the reflected GNSS signal is coming from close to nadir, most of the reflected signal will change its polarization to LHCP. At the Brewster angle, the power of the reflected RHCP and LHCP is equal. Since the Brewster angle depends on the dielectric properties of the surface, it has to be measured for each reflective surface (see Fig. 8.3). Different phases of water have Brewster angles in the interval between 54 degree for dry snow (blue curves) and 83 degree for seawater. The Brewster angle for seawater can itself vary between 58 degree and 85 degree, depending on water salinity and density (Jin, Cardellach, & Xie, 2014).

The standard GNSS antennas and receivers, used for positioning and geodesy, are capable of receiving RHCP signals only. Dedicated LHCP antennas and receivers are developed specifically to observe reflected signals. Such receivers are not widely available and are primarily used in the scientific ground-based stations (described in “Ground-based GNSS-R measurements” section), or on satellites and aircraft.

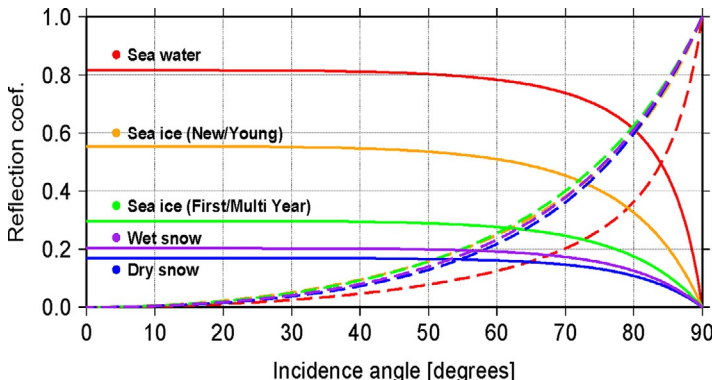


Fig. 8.3 The solid lines show the reflection coefficient R of the LHCP reflected signal at incidence angles between 0 degree and 90 degree for seawater, ice, and snow. The dashed lines show the reflection coefficient for the RHCP reflected signal. The Brewster angles for each reflecting surface are at the intersection between the solid and dashed lines. This figure shows that different phases of water have Brewster angles in the interval between 54 degree for dry snow (blue curves; dark gray in print version) and 83 degree for seawater. (From Jin, S., Cardellach, E., & Xie, F. (2014). *GNSS remote sensing*. Springer.)

GNSS-R wind speed measurements

Specular and diffuse scattering

The theoretical basis for GPS signals scattering from the ocean surface through the Bistatic Radar Equation was proposed ([Zavorotny & Voronovich, 2000](#)). The roughness of the reflective surface plays an important role in the way a receiver reads the reflected signals. In an ideal case, when the reflective surface is smooth, the reflected signal received by the observer originates in a single point (specular reflection). In reality, the surface of the Earth is rough and the reflected signal received by the observer originates from a glistening zone ([Fig. 8.4](#)). The size of the zone depends on the roughness of the surface.

When the GNSS signal is reflected from a smooth surface, the receiver observes two navigation messages—one coming directly from the satellite and the other from the reflective surface. The excess path of the reflected signal is determined through the cross correlation between the received direct signal binary code from the satellite and the binary code of the reflected signal. Since the reflection is specular, the waveform of the correlator output for the reflected signal is the same as the waveform for the direct signal (see [Fig. 8.5](#)) and has triangular function of half-width equal to the travel time of a single code chip.

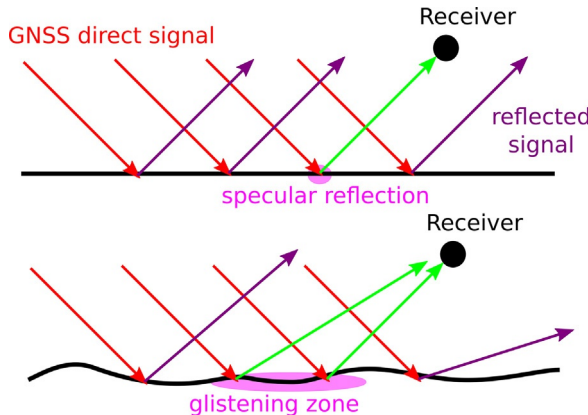


Fig. 8.4 Glistening. The reflective surface on top is flat and smooth, which means that the observer receives reflection from a single point. When the roughness of the reflective surface increases, the observer receives reflected signals from multiple points within a glistening zone. The higher the roughness, the larger the glistening zone.

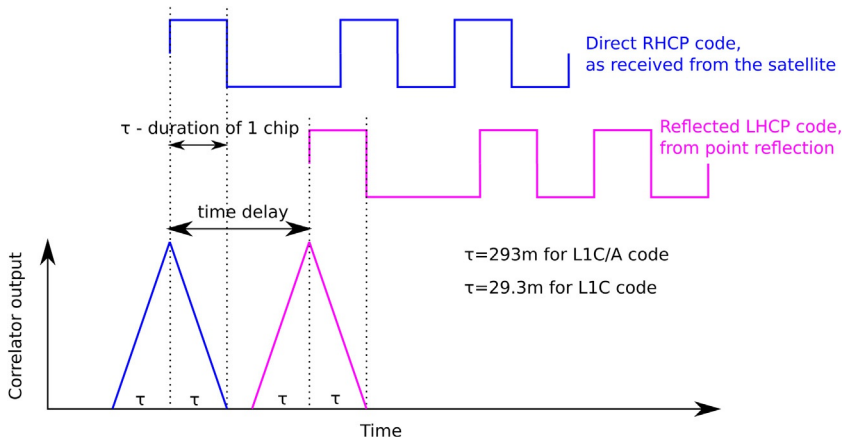


Fig. 8.5 Specular reflection. The waveform of the reflected signal from a specular reflection is identical to the waveform of the direct signal. The width of the waveform is double the time duration of one code chip.

When the GNSS signal is reflected from a rough surface, the signal travels a distance different from the satellite to the receiver than when it is reflected from the center facets of the glistening zone, compared to the reflections, coming from the facets at the edges of the glistening zone. Since the signal is traveling at a constant speed, the longer travel distance is observed by the

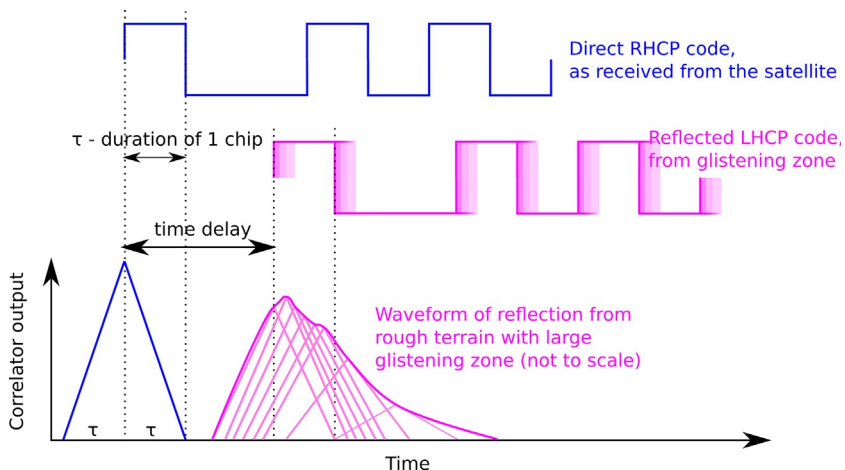


Fig. 8.6 Glistening waveform. The waveform of a reflected signal from a rough surface is prolonged since reflections from multiple facets within the glistening zone are received. The larger the glistening zone, the wider the waveform.

receiver as a delay. Each reflection facet contributes its own delayed copy of the original signal code. All of these copies are received in the receiver with incremental delays. These delays contribute to a prolonged waveform, demonstrating the longer time that the reflected signals take to reach the receiver. The higher the roughness of the reflective surface, the flatter the waveform (see Fig. 8.6).

Since the GNSS signals are transmitted from a moving satellite, reflected from a quasistationary surface and received on a moving platform, Doppler shifts in the frequency of the received signals are observed. A separate waveform can be observed for each Doppler belt, thus creating a Doppler-delay map (DDM) of the reflection (see Fig. 8.7).

Spaceborne wind speed measurements

The scientific principle employed in wind speed measurements from dedicated LEO satellites, equipped with GNSS-R receivers, is based on the increased roughness of the sea surface. The stronger the blowing wind, the higher the surface roughness. In 2002 the first reflected GPS signal was received from space through the Spaceborne Imaging Radar-C (SIR-C) (Lowe et al., 2002). The first satellite, equipped with a GNSS-R receiver, is the UK Disaster Monitoring Constellation (UK-DMC), which

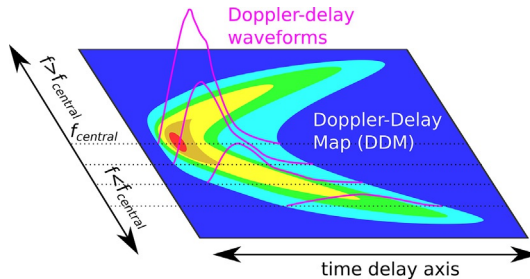


Fig. 8.7 DDM. The Doppler-delay maps are visual representations of the waveforms of a reflection, stacked along the frequency Doppler axis (y axis) and are color coded for intensity. The higher the roughness of the reflective surface, the larger the footprint of the reflection on the DDM.

was launched in 2003. During this mission, the first wind speed measurements were derived through GNSS-R measurements (Gleason et al., 2005). In 2014 the first dedicated GNSS-R mission was launched—the TechDemoSat-1 (TDS-1). The TDS-1 mission was followed in 2016 by the eight satellite Cyclone GNSS (CYGNSS) mission for tropical cyclone forecasting and hurricane tracking (Ruf et al., 2018).

The method of measuring wind speed from DDMs (Fig. 8.8) relies on creating a Geophysical Mapping Function (GMF). The Geophysical Mapping Function should not be confused with Global Mapping Function (also marked as GMF), which is used in positioning. The GMF is a function, designed to relate the waveforms from the DDMs to wind speed observations. The training of these generally empirical GMFs is based on using supplementary data from global reanalysis (such as ERA5 or ERA-Interim), or satellite measurements from missions, such as the Advanced SCATterometer (ASCAT) (Asgarimehr, Zavorotny, Wickert, & Reich, 2018). In figure GMF, DDM cross sections from the TDS-1 satellite are plotted against 10-m wind speeds from ERA-Interim. The red line (dark gray in print version) indicates the fitted exponential GMF. The indicated bias between the ERA-Interim and GNSS-R wind speeds is 0.23 m/s with RMSE of 2.76 m/s (Fig. 8.9).

The experiments with measuring wind speed using GNSS-R have shown absolute biases between GNSS-R measurements and ASCAT in the range of 0–1.5 m/s and RMSE of 1–4 m/s. The exponential form of the GMFs suggests that the GNSS-R observations of wind speed are far more sensitive at wind speeds below 15 m/s, than at higher wind speeds.

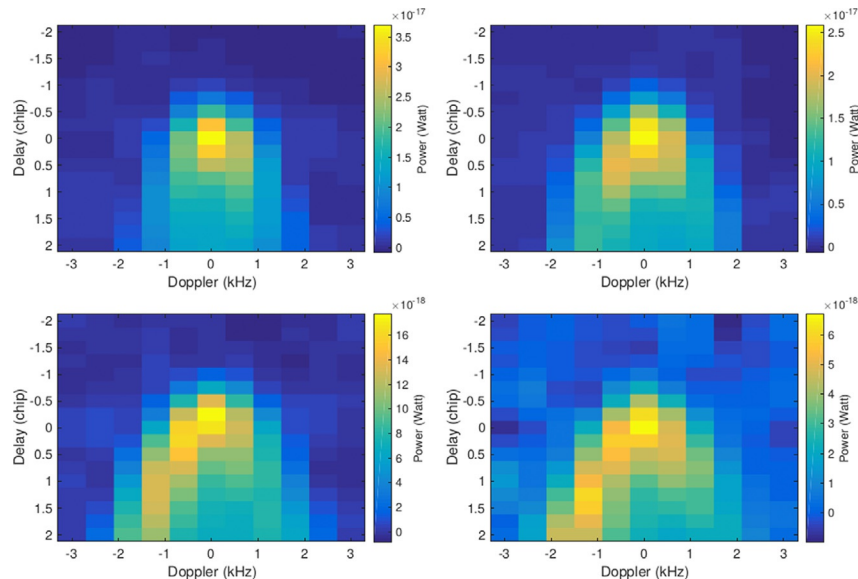


Fig. 8.8 DDM's for wind. Exemplary DDMs at wind speeds of 1.5 m/s (top left), 3.7 m/s (top right), 4.5 m/s (bottom left), and 8.3 m/s (bottom right). (From Asgarimehr, M. (2020). Spaceborne GNSS Reflectometry: Remote Sensing of Ocean and Atmosphere. In Technische Universität Berlin. Technische Universität Berlin.)

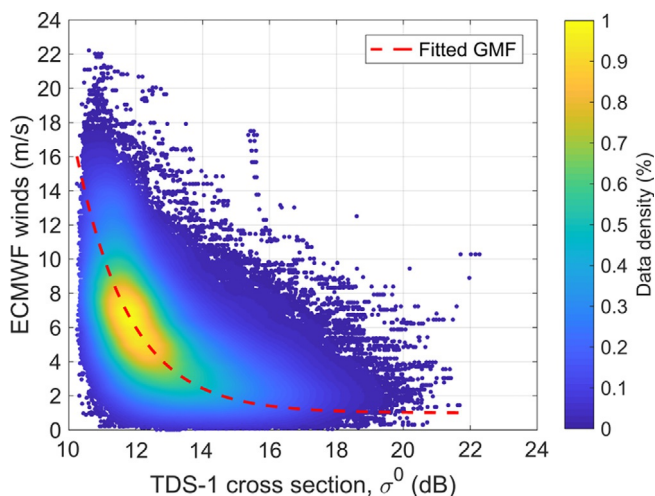


Fig. 8.9 GMF. DDM cross sections from the TDS-1 satellite plotted against 10-m wind speeds from ERA-Interim. The red line (dark gray in print version) indicates the fitted exponential GMF. (From Asgarimehr, M., Wickert, J., & Reich, S. (2018). TDS-1 GNSS reflectometry: Development and validation of forward scattering winds. IEEE Journal of Selected Topics in Applied Earth Observations and Remote Sensing, 11(11), 4534–4541.)

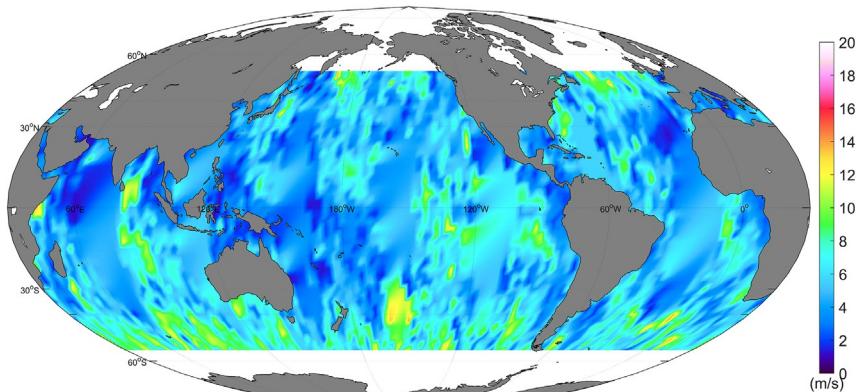


Fig. 8.10 Wind world. Average global wind speed (May 2015 to June 2016) by TDS-1 SGR-ReSI measurements. (From Asgarimehr, M., Wickert, J., & Reich, S. (2018). TDS-1 GNSS reflectometry: Development and validation of forward scattering winds. *IEEE Journal of Selected Topics in Applied Earth Observations and Remote Sensing*, 11(11), 4534–4541.)

Additionally, the sea roughness is affected not only by the blowing wind but also by the splashes of raindrops on the sea surface, which brings additional uncertainty to the final wind speed measurements (Asgarimehr, Wickert, & Reich, 2018). The greatest advantage of the GNSS-R measured wind speeds is the high spatiotemporal resolution of measurements, provided by the growing constellation of GNSS-R satellites (see Fig. 8.10).

GNSS-R water level/land height measurements

Carrier-phase measurements

Phase altimetry relies on measuring distance differences based on phase change and the number of full phase cycles, each of them representing a distance change of 1 wavelength

$$\Delta\phi = \frac{1}{\lambda} p_H + v, \quad (8.3)$$

where $\Delta\phi$ is the phase change, λ is the wavelength, p_H is the path for a specific height, and v are residuals. By having two receivers, one RHCP upward-looking and another LHCP downward- or side-looking, the difference in height between these two receivers can be calculated through the path difference between the two receivers. The change in the path difference can be monitored through the change in the carrier phase.

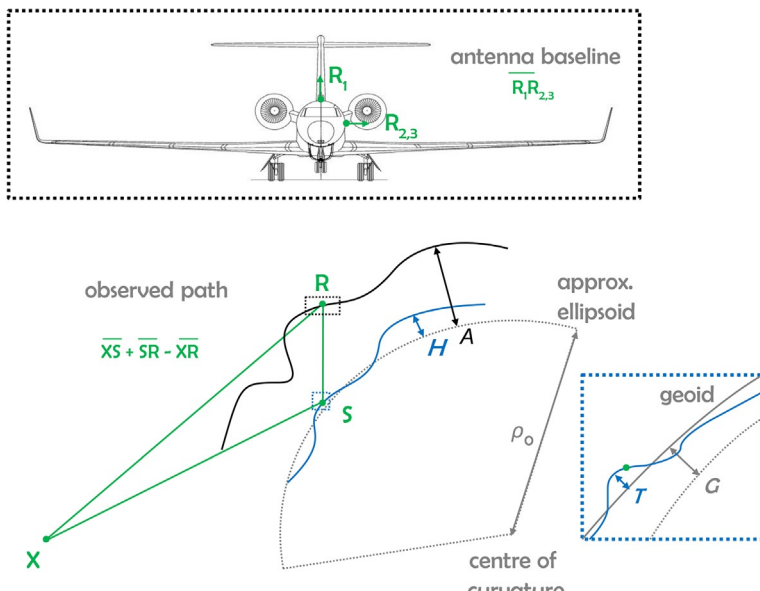


Fig. 8.11 HALO. This figure shows the location of the zenith-looking and side-looking GNSS antenna onboard the HALO aircraft during a measurement campaign over Italy. Below the geometry of the GNSS signals is presented. (Reproduced from Semmling, A., Beckheinrich, J., Wickert, J., Beyerle, G., Schön, S., Fabra, F., Pflug, H., He, K., Schwabe, J., & Scheinert, M. (2014). Sea surface topography retrieved from GNSS reflectometry phase data of the GEOHALO flight mission. *Geophysical Research Letters*, 41(3), 954–960.)

Sea level measurements with airborne GNSS-R

Airborne GNSS Reflectometry uses the carrier-phase GNSS-R. Unlike the spaceborne systems, the receivers are mounted on an aircraft, such as the High Altitude and Long Range Research Aircraft (HALO), with two antennas, one looking in zenith and the second one in nadir direction (Fig. 8.11).

This method is used for observation campaigns, where reflections from specific areas are of interest. Such campaigns have been carried out for water level measurements over the lake Konstanz (Semmling, Beckheinrich, et al., 2014) and sea level and wind speed measurements over the southern coast of Italy (see Fig. 8.12) (Semmling, Schön, et al., 2014). These campaigns have been used both for measurements over specific regions and for proof-of-concept missions for GNSS-R.

The experiment over the coast of Italy shows very good agreement between the GNSS-R-derived sea altimetry data and the Mean Sea Surface height from the DTU-10 ellipsoid observations (Fig. 8.13). The reported accuracy for some of the measured tracks in the figure map of Italy is below 10 cm.

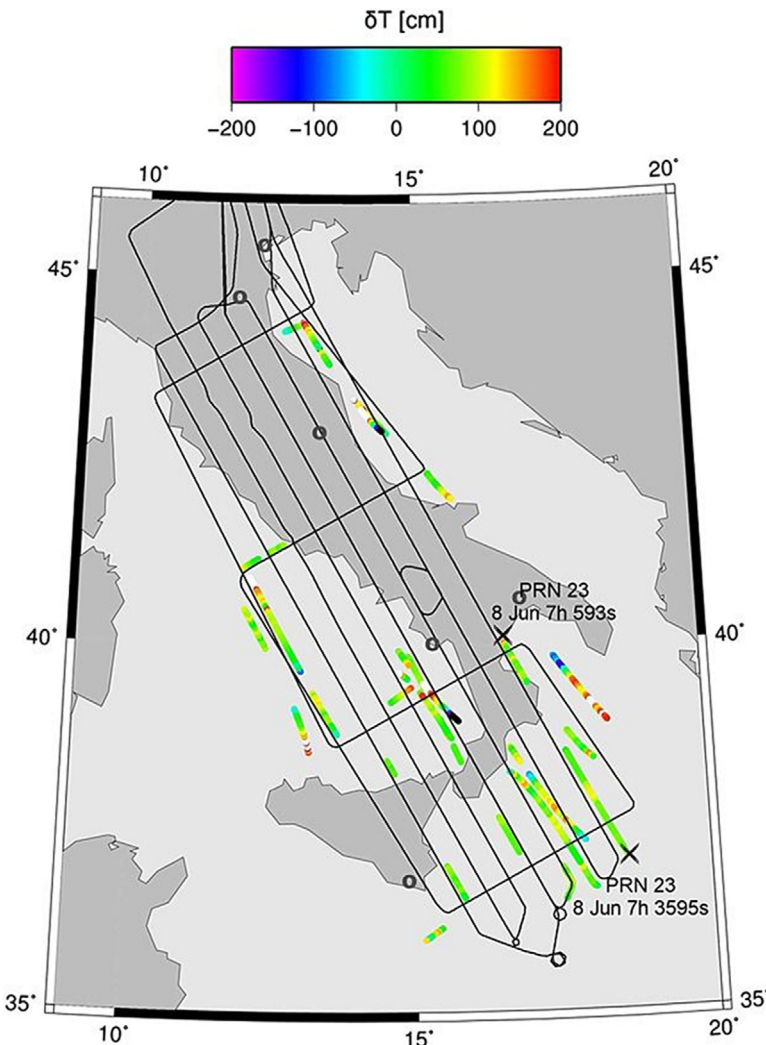


Fig. 8.12 Map Italy. This map shows the HALO plane flybys over Italy and the colored tracks represent the observed GPS reflections from the sea surface. (From Semmling, A., Beckheinrich, J., Wickert, J., Beyerle, G., Schön, S., Fabra, F., Pflug, H., He, K., Schwabe, J., & Scheinert, M. (2014). Sea surface topography retrieved from GNSS reflectometry phase data of the GEOHALO flight mission. *Geophysical Research Letters*, 41(3), 954–960.)

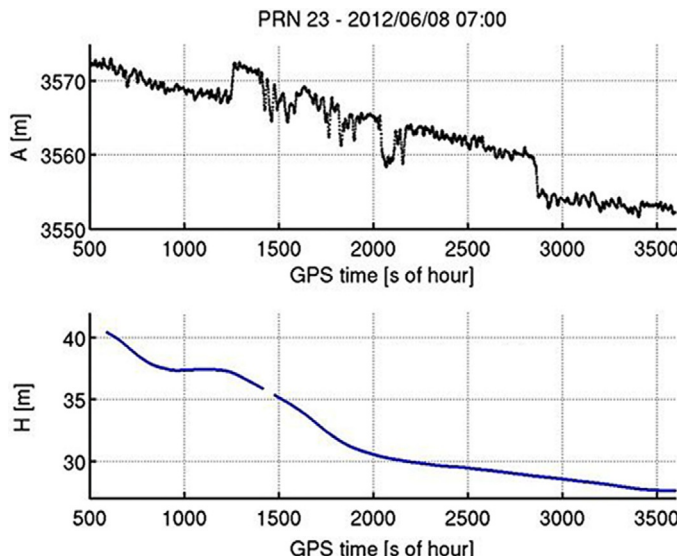


Fig. 8.13 Italy results. The top figure represents the reflections from GPS PRN23 satellite. The bottom figure is the mean sea surface height over the same path, as the PRN23 reflection. (From Semmling, A., Beckheinrich, J., Wickert, J., Beyerle, G., Schön, S., Fabra, F., Pflug, H., He, K., Schwabe, J., & Scheinert, M. (2014). Sea surface topography retrieved from GNSS reflectometry phase data of the GEOHALO flight mission. *Geophysical Research Letters*, 41(3), 954–960.)

The retrievals are carried out at elevation angles between 10° and 30° since the method postulates specular reflections and higher elevation angles are more dependent on sea roughness (Semmling, Beckheinrich, et al., 2014).

Ground-based GNSS-R measurements

Apart from airborne GNSS-R observations can be also performed with ground-based GNSS stations. Experiments in the Onsala Observatory in Sweden proved the concept of using a zenith-looking RHCP antenna, parallel to a nadir-looking LHCP antenna to perform carrier-phase observations, similar to the airborne altimetry methodology. In the same study, the RHCP antenna was also used to record SNR data (described in more detail in “GNSS-R soil moisture monitoring” section) to measure the height of the reflective surface. The results from these experiments are then compared to the tide gauge, installed near the GNSS setup (Fig. 8.14).

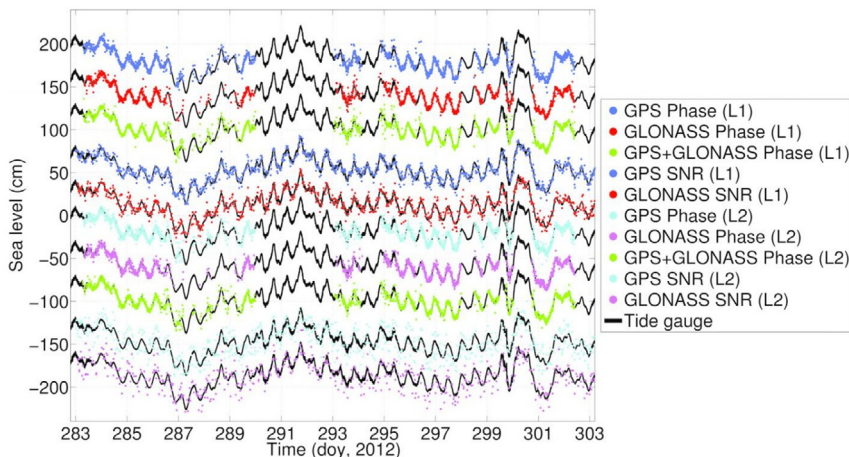


Fig. 8.14 Onsala. Sea level height from tide gauge (in black) over a period of 20 days at Onsala Observatory are compared with GNSS reflectometry observations (in color) from several GNSS combinations and two reflector height retrieval techniques—carrier phase and SNR. (Löfgren, J. S., & Haas, R. (2014). *Sea level observations using multisystem GNSS reflectometry*. NKG, 17th General Assembly.)

The results from this experiment show (see Fig. 8.14) that both carrier-phase observations from the dual setup and SNR observations from the RHCP zenith antenna provide accurate measurements of the tides in the area of observation (Löfgren & Haas, 2014). The correlation between the GNSS-R measurements and the tide gauge is between 0.85 and 0.95 for the different methods and combinations of different GNSSs. The study also shows that the SNR observations have 1.5–3 times higher standard deviation from the tide gauge compared to the results from the carrier-phase observations.

GNSS-R soil moisture monitoring

The soil can be separated into several different layers, based on porosity, presence of organic matter, and structure. The layers in the soil are named horizons (Fig. 8.12). The soil layer, located in the top 20 cm of the soil profile is the O horizon (O stands for Organic). The O horizon is rich in organic particles, holds the root structure of the low vegetation, and is very porous. The following A (20–50 cm) and B (50 cm–3 m) horizons are denser, less porous, and host the roots of trees. The C horizon (3–5 m) is the soil layer just above the bedrock. This is usually the layer where groundwater is found. When speaking

about soil moisture, hydrologists usually consider the amount of water in the O, A, and B horizons. GNSS signals, however, get reflected from the O horizon, so the soil moisture, measured through GNSS-R, is only relevant to the topsoil, i.e., top 15 cm (Brady & Weil, 2013).

The most widely used soil moisture metrics are (1) specific water content (SWC), which is the fraction of the water mass from the mass of a confined amount of soil, and (2) volumetric water content (VWC), which is the fraction of the water volume in a confined volume of soil. VWC can be measured in both $[\text{cm}^3_{\text{H}_2\text{O}}/\text{cm}^3_{\text{soil}}]$ or in $[\text{Vol}\%]$, where the absolute values have the following relation: $1[\text{cm}^3_{\text{H}_2\text{O}}/\text{cm}^3_{\text{soil}}] = 100[\text{Vol}\%]$. Another soil moisture metric is the relative water content (RWC), which represents the volume of water present in the soil as a fraction of the saturated water amount in the soil. RWC is measured in [%] (Simeonov, 2021).

Single-antenna SNR observations

When the direct and reflected GNSS signals reach the ground antenna, they are both detected. The signal strength of the direct and the reflected signal, as received by the antenna, depends on the elevation angle of the GNSS satellite (through the Brewster law dependence) and on the GNSS antenna gain pattern (Larson et al., 2008). Since reflected signals are usually regarded as noise, geodetic antennas are equipped with noise-canceling choke rings (specially designed metal collars, which block the reflected signals). The antenna cannot distinguish the direct signal from the reflected, the recorded signal strength shows the interference pattern between these two signals (as shown in Fig. 8.15). The reason for the occurrence of the interference pattern is that there is a periodicity in the phase difference between the direct and reflected signals (Fig. 8.16). When the direct and reflected signals are in-phase, the resulting amplitude of the received signal strength is amplified. When the two signals are in the counter phase, the signal strength, as received by the antenna, is damped. The term signal strength is used as a description of the direct signal in units of dB—Hz.

The resulting signal strength interference pattern is polynomially detrended and subsequently, the low elevation angles of the signal-to-noise ratio (SNR) is acquired and analyzed. The SNR can be modeled with the following equation:

$$\text{SNR} = A \cos \left(\frac{4\pi h}{\lambda} + \phi \right) \quad (8.4)$$

where A is the average amplitude of the interference pattern, h is the height difference between the antenna and the reflective surface, λ is the frequency

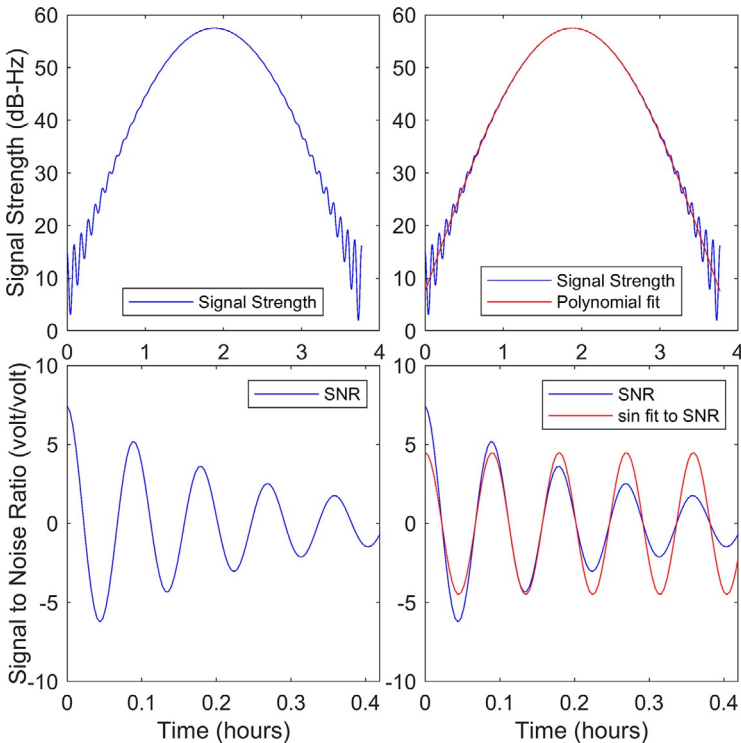


Fig. 8.15 Single antenna reflection. *Top left* is the theoretical signal strength, observed by a ground-based station for a GPS satellite transit. A second-order polynomial fit is used to simulate the signal strength observations without the reflection interference (*top right*). The difference between the observed and the polynomial fit represents the SNR interference pattern (*bottom left*), the period and amplitude of which are estimated through an LSA sinusoidal fit (*bottom right*). (From Simeonov, T. (2021). *Derivation and analysis of atmospheric water vapor and soil moisture from ground-based GNSS stations*. In Technische Universität Berlin. Technische Universität Berlin.)

of the signal, e is the elevation angle of the satellite, ϕ is a phase shift, and the SNR is the result of the detrending of the signal strength and is measured in (volt/volt). Fig. 8.15 (bottom left and right) shows that the amplitude depends on the elevation angle.

The amplitude and phase shift of the SNR are estimated using a Lomb-Scargle least-squares adjustment (LSA). Every sampled frequency is represented in the spectrum of significance, where the highest significance is given to the lowest least-squares difference between the sample and the fitted curve.

This SNR methodology enables the measurement of reflector height changes (used in “Ground-based GNSS-R measurements” section), as well as soil moisture observations through the changes of the phase ϕ .

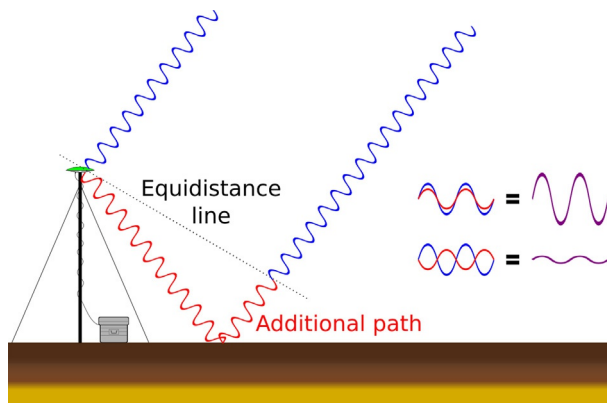


Fig. 8.16 SNR distance. The GNSS antenna cannot distinguish the direct from the reflected RHCP signal. Thus the antenna records the interference between the direct and reflected signals in the signal strength observation. (From Simeonov, T. (2021). *Derivation and analysis of atmospheric water vapor and soil moisture from ground-based GNSS stations*. In Technische Universität Berlin. Technische Universität Berlin.)

The GNSS signal path is usually described as a straight line (direct optical path). In reality, the signal propagation between the GNSS satellite and the receiver forms an electromagnetic wave front (Fig. 8.17). The prolate spheroid volume, encapsulating semicoherent signals with phase shifts up to 90 degree from the direct optical path, is the first Fresnel zone (visualized in Fig. 8.17). The section of the first Fresnel zone of a reflected signal has an elliptical shape (see Fig. 8.18).

SNR soil moisture monitoring with single-antenna GNSS-R

The soil moisture estimations are extracted from the phase shifts of the SNR data. (Chew, Small, Larson, & Zavorotny, 2014) estimated that the change of 0.65° in the phase shift of the SNR is equivalent to a 1 Vol% change of soil moisture. Since the relation between the two parameters is linear, a dataset with the phase changes can be created

$$\Delta\phi = \phi - \phi_0 \quad (8.5)$$

where ϕ_0 is the minimum phase shift of the SNR for the entire dataset. From this the volumetric water content (VWC) of the soils can be estimated as follows:

$$VWC = \frac{\Delta\phi}{\gamma} + c_{min} \quad (8.6)$$

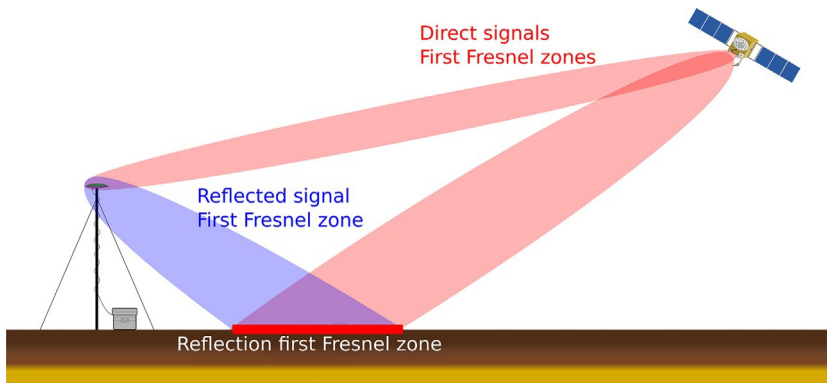


Fig. 8.17 Fresnel. First Fresnel zones of direct and reflected signals. The section of the reflected first Fresnel zone indicates the area of signal reflection at the surface. This is not to be confused with the reflection glistening zone, discussed in “Theoretical background—Polarization” section. (Reproduced from Simeonov, T. (2021). Derivation and analysis of atmospheric water vapor and soil moisture from ground-based GNSS stations. In Technische Universität Berlin. Technische Universität Berlin.)

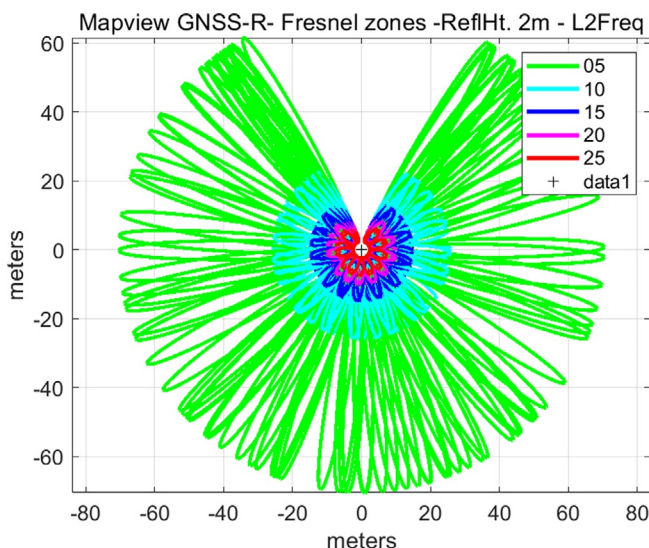


Fig. 8.18 Fresnel ground. This is a figure of the Fresnel zones of reflection for a 2-m high antenna above ground (marked with a cross in the center) and for elevation angles between 5 degree (green ellipses; dark gray in print version) and 25 degree (red ellipses; dark gray in print version). The area covered by these reflections is about 500 m².

where c_{min} is a constant, equal to the minimum soil moisture or residual soil moisture. The value of c_{min} is station specific and is within the range 3.5–5 Vol%. Apart from a minimum possible value for soil moisture, there is also a saturation soil moisture value. The saturation soil moisture is estimated to be 60 ± 10 Vol%, depending on the soil type (Brady & Weil, 2013).

A study at an experimental site in Germany (Marquardt) shows that the soil moisture retrievals from a ground-based GNSS station are comparable to soil moisture measurements performed by Time Domain Reflectometry (TDR). The correlation between the two methods shows variability between the different seasons and is in the range between 0.5 and 0.9 with higher correlations in the summer periods and lower in winter. The seasonality is explained by several factors, among which the freezing of the soil during cold winters with no snow cover. It is to be noted that there is high correlation between precipitation events (blue bars) and local maxima of soil moisture. The TDR measurements during late August and September (Fig. 8.19) show much lower soil

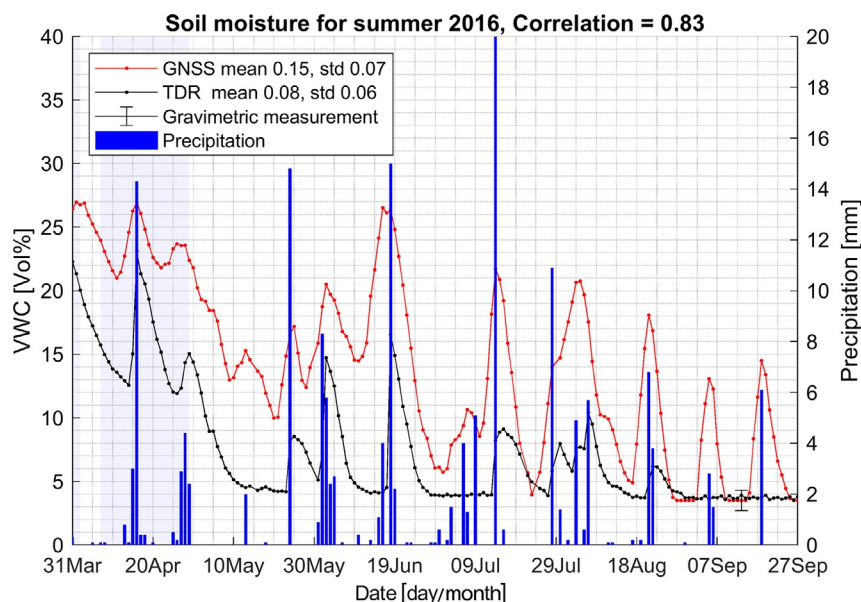


Fig. 8.19 Marquardt. Soil moisture measurements from GNSS-R (in red; dark gray in print version) and TDR (in black) for the summer months of 2016 at GNSS station Marquardt, Germany. Precipitation is plotted in blue bars (dark gray in print version). (From Simeonov, T. (2021). Derivation and analysis of atmospheric water vapor and soil moisture from ground-based GNSS stations. In Technische Universität Berlin. Technische Universität Berlin.)

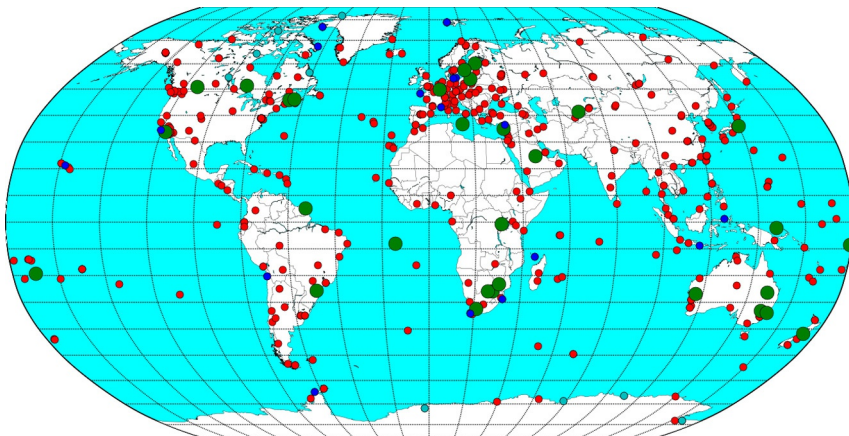


Fig. 8.20 IGS. The stations, marked with the large green dots (large dark gray in print version) indicate sites, where GNSS-R soil moisture observations have been made. The sites marked with blue (dark gray in print version) and cyan (light gray in print version) indicate sites where water level and snow height retrievals through SNR can be performed. In the sites, marked with red dots (dark gray in print version), no SNR GNSS-R retrievals of environmental parameters are possible. (From Simeonov, T. (2021). *Derivation and analysis of atmospheric water vapor and soil moisture from ground-based GNSS stations*. In Technische Universität Berlin. Technische Universität Berlin. Global map of all IGS sites.)

moisture, compared to the GNSS-R. This is due to the difference in the sampling area of the two methods (Simeonov, 2021).

In another study, the feasibility of using the International GNSS Service network for soil moisture retrievals is studied. The analysis shows that out of more than 500 stations, only around 30 stations can be used for reflectometry using the SNR observations methodology (see Fig. 8.20). The stations, where soil moisture observations have been successfully performed, cover all climate zones and continents. The soil moisture retrievals are highly dependent on local area conditions and the locations of the GNSS sites (Simeonov, 2021).

Spaceborne soil moisture monitoring with GNSS-R

The spaceborne soil moisture observations are carried on LEO satellites with GNSS-R receivers, described in the spaceborne wind measurement retrievals over oceans. Since the GNSS-R receivers can record reflections, coming not only from the sea surface but also from the ground, the reflections can be used to monitor properties of the land. Unlike the wind speed

measurements, where DDMs are used, the spaceborne soil moisture monitoring uses the forward scattered signal power ($P_{r, \text{eff}}$). Studies have shown that the effective forward scattered signal power of wet surfaces produce stronger reflections than dry surfaces (Chew et al., 2014). Wetter surfaces have higher dielectric constants, which results in higher reflectivity than drier surfaces (Egido et al., 2012). Fig. 8.21 presents the $P_{r, \text{eff}}$ (left) and soil moisture VWC (right) for May (top), August (center), and the difference (bottom) (Chew & Small, 2018). The VWC measurements are from the Soil Moisture Active Passive (SMAP) satellite.

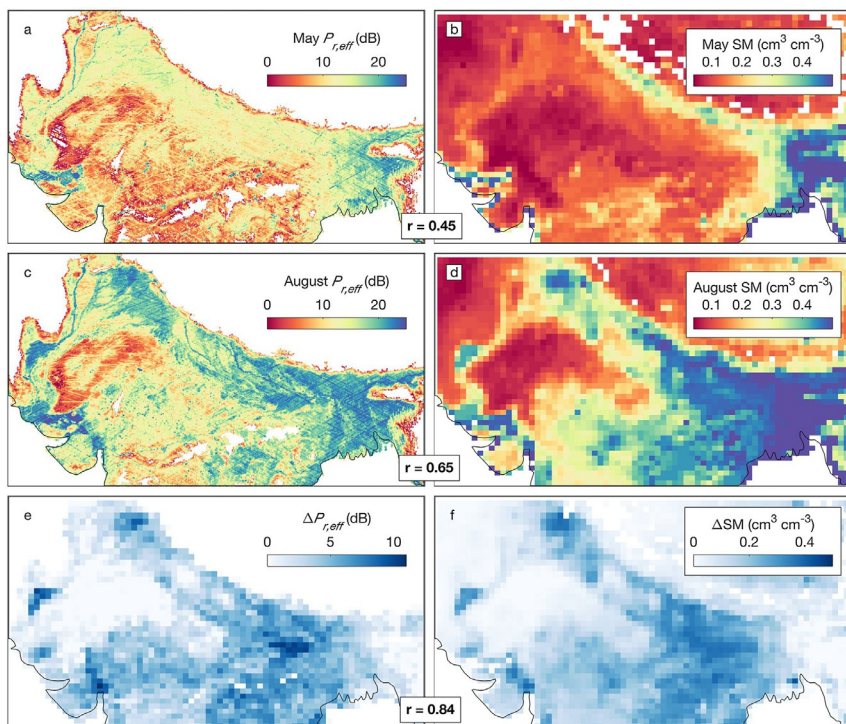


Fig. 8.21 India. (Left) Reflected power from the land, as recorded by the CYGNSS satellites constellation. (Right) The corresponding VWC measurements from the SMOS and SMAP satellites. (Middle) The spatial correlation between the two figures is recorded. (From Chew, C., & Small, E. (2018). Soil moisture sensing using spaceborne GNSS reflections: Comparison of CYGNSS reflectivity to SMAP soil moisture. *Geophysical Research Letters*, 45(9), 4049–4057.)

References

- Asgarimehr, M., Wickert, J., & Reich, S. (2018). TDS-1 GNSS reflectometry: Development and validation of forward scattering winds. *IEEE Journal of Selected Topics in Applied Earth Observations and Remote Sensing*, 11(11), 4534–4541.
- Asgarimehr, M., Zavorotny, V., Wickert, J., & Reich, S. (2018). Can GNSS reflectometry detect precipitation over oceans? *Geophysical Research Letters*, 45(22), 12–585.
- Brady, N. C., & Weil, R. (2013). *Nature and properties of soils, the: Pearson new international edition*. Pearson Higher Ed.
- Chew, C., & Small, E. (2018). Soil moisture sensing using spaceborne GNSS reflections: Comparison of CYGNSS reflectivity to SMAP soil moisture. *Geophysical Research Letters*, 45(9), 4049–4057.
- Chew, C. C., Small, E. E., Larson, K. M., & Zavorotny, V. U. (2014). Vegetation sensing using GPS-interferometric reflectometry: Theoretical effects of canopy parameters on signal-to-noise ratio data. *IEEE Transactions on Geoscience and Remote Sensing*, 53(5), 2755–2764.
- Egido, A., Caparrini, M., Ruffini, G., Paloscia, S., Santi, E., Guerriero, L., et al. (2012). Global navigation satellite systems reflectometry as a remote sensing tool for agriculture. *Remote Sensing*, 4(8), 2356–2372.
- Gleason, S., Hodgart, S., Sun, Y., Gommenginger, C., Mackin, S., Adjrad, M., et al. (2005). Detection and processing of bistatically reflected GPS signals from low earth orbit for the purpose of ocean remote sensing. *IEEE Transactions on Geoscience and Remote Sensing*, 43(6), 1229–1241.
- Jin, S., Cardellach, E., & Xie, F. (2014). *GNSS remote sensing*. Springer.
- Larson, K. M., Small, E. E., Gutmann, E. D., Bilich, A. L., Braun, J. J., & Zavorotny, V. U. (2008). Use of GPS receivers as a soil moisture network for water cycle studies. *Geophysical Research Letters*, 35(24).
- Löfgren, J. S., & Haas, R. (2014). Sea level observations using multi-system GNSS reflectometry. In *NKG, 17th general assembly*.
- Lowe, S. T., LaBrecque, J. L., Zuffada, C., Romans, L. J., Young, L. E., & Hajj, G. A. (2002). First spaceborne observation of an Earth-reflected GPS signal. *Radio Science*, 37(1), 1–28.
- Martin-Neira, M. (1993). A passive reflectometry and interferometry system (PARIS): Application to ocean altimetry. *ESA Journal*, 17(4), 331–355.
- Ruf, C. S., Chew, C., Lang, T., Morris, M. G., Nave, K., Ridley, A., et al. (2018). A new paradigm in earth environmental monitoring with the CYGNSS small satellite constellation. *Scientific Reports*, 8(1), 1–13.
- Semmling, A., Beckheinrich, J., Wickert, J., Beyerle, G., Schön, S., Fabra, F., et al. (2014). Sea surface topography retrieved from GNSS reflectometry phase data of the GEO-HALO flight mission. *Geophysical Research Letters*, 41(3), 954–960.
- Semmling, M., Schön, S., Beckheinrich, J., Beyerle, G., Ge, M., & Wickert, J. (2014). Carrier phase altimetry using Zeppelin based GNSS-R observations and water gauge reference data. In *EGUGA* (p. 11787).
- Simeonov, T. (2021). Derivation and analysis of atmospheric water vapour and soil moisture from ground-based GNSS stations. In *Technische Universität Berlin Technische Universität Berlin*.
- Zavorotny, V. U., & Voronovich, A. G. (2000). Scattering of GPS signals from the ocean with wind remote sensing application. *IEEE Transactions on Geoscience and Remote Sensing*, 38(2), 951–964.